Experimental observations of the squeezing-to-dripping transition in T-shaped microfluidic junctions

Gordon F. Christopher, N. Nadia Noharuddin, Joshua A. Taylor, and Shelley L. Anna*
Department of Mechanical Engineering, Carnegie Mellon University, Pittsburgh, Pennsylvania 15213, USA
(Received 25 March 2008; published 18 September 2008)

An experimental study of droplet breakup in T-shaped microfluidic junctions is presented in which the capillary number and flow rate ratio are varied over a wide range for several different viscosity ratios and several different ratios of the inlet channel widths. The range of conditions corresponds to the region in which both the squeezing pressure that arises when the emerging interface obstructs the channel and the viscous shear stress on the emerging interface strongly influence the process. In this regime, the droplet volume depends on the capillary number, the flow rate ratio, and the ratio of inlet channel widths, which controls the degree of confinement of the droplets. The viscosity ratio influences the droplet volume only when the viscosities are similar. When there is a large viscosity contrast in which the dispersed-phase liquid is at least 50 times smaller than the continuous-phase liquid, the resulting size is independent of the viscosity ratio and no transition to a purely squeezing regime appears. In this case, both the droplet volume and the droplet production frequency obey power-law behavior with the capillary number, consistent with expectations based on mass conservation of the dispersed-phase liquid. Finally, scaling arguments are presented that result in predicted droplet volumes that depend on the capillary number, flow rate ratio, and width ratio in a qualitatively similar way to that observed in experiments.

DOI: 10.1103/PhysRevE.78.036317 PACS number(s): 47.61.−k, 47.55.db

I. INTRODUCTION

Numerous important industries rely on the ability to synthesize liquid droplets, gas bubbles, and solid particles, including inkjet printing, pharmaceuticals for drug delivery, and consumer products. Methods for synthesizing droplets are as numerous as the applications, but microfluidic techniques have recently become popular due to their ability to generate highly uniform particles. Several microfluidic geometries have been developed to synthesize uniform particles, including T-shaped junctions [1–4], coflowing configurations [5,6], and flow-focusing geometries [7–10]. These configurations and the underlying droplet breakup mechanisms are described in detail in a recent review [11]. The emergence of microfluidic methods has given rise to new applications for highly uniform particles, including the synthesis of novel multicomponent emulsions [6,12] and nonspherical solid microparticles [12–15] as well as the use of the droplets themselves as discrete reactors within lab-on-a-chip devices [16,17].

Despite numerous studies investigating mechanisms for droplet breakup in microfluidic devices, physical models predicting the droplet size, uniformity, and production frequency as a function of all the relevant control parameters are lacking. This deficiency arises in part from a lack of comprehensive experimental observations spanning the available phase space. To address this need, the present work describes a systematic experimental study of droplet breakup in T-junctions, focusing on conditions that lie in the transition region between the squeezing and dripping regimes that have been studied previously [1,4,18].

In a microfluidic T-junction, two immiscible liquids flow into separate inlet channels that meet at right angles, as shown in Fig. 1. The liquid to be dispersed emerges into the junction, and the cross-flow of the second continuous-phase liquid deforms the emerging interface and leads to breakup of discrete droplets. Liquid flow is commonly controlled via independent syringe pumps imposing volumetric flow rates Q_d and Q_c in each liquid. A small number of studies have reported controlling the inlet pressures P_d and P_c using pressure regulators [2,19]. The relevant geometric parameters in a T-channel include the widths of the two inlet channels,

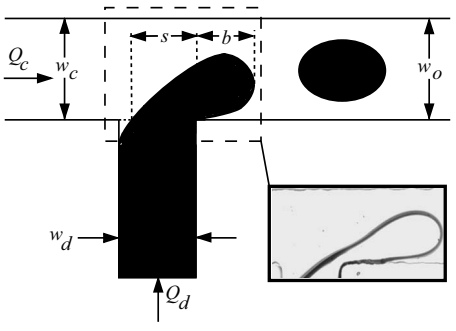

FIG. 1. Schematic diagram of a microfluidic T-junction. The width of the channel into which the continuous-phase liquid flows at a rate Q_c is denoted w_c, while the width of the channel into which the dispersed-phase liquid flows at a rate Q_d is denoted w_d. Soft lithography fabrication leads to a uniform depth h throughout the device. The inset shows a typical image of a droplet emerging from the inlet channel and deforming due to the cross-flow of the continuous-phase liquid. The droplet emerges until it reaches a length b and a neck thickness s, as measured from the downstream corner of the T-junction. Cross-flow of the continuous-phase liquid then forces the droplet neck to thin, during which time the droplet continues to grow due to injection of the dispersed-phase liquid.

*Author to whom correspondence should be addressed. sanna@cmu.edu

denoted w_d and w_c, respectively, and the width of the outlet channel, w_o. In the present study, the width of the outlet channel is identical to that of the continuous-phase inlet, $w_o = w_c$. Fabrication constraints lead to channels with rectangular cross section in which the channel depth h is uniform throughout the device. Also, the dispersed-phase liquid must be nonwetting relative to the continuous-phase liquid for the stable production of droplets [20].

Three main fluid stresses act on the emerging interface and influence droplet breakup in a T-junction [1,4]. Viscous shear stress due to cross-flow of the continuous-phase liquid deforms the interface. The magnitude of the viscous shear stress is estimated by the product $\mu_c G$, where μ_c is the viscosity of the continuous-phase liquid and G is a characteristic rate of shear strain that is proportional to Q_c and is a function of the T-junction geometry and that of the emerging interface. The interfacial tension resists deformation by establishing a pressure jump $(p_d - p_c) \sim \sigma\kappa$ across the curved interface of the growing droplet that is proportional to the curvature κ and the interfacial tension σ. Finally, as the emerging interface fills the junction, the available area through which fluid can pass is restricted, leading to an increased pressure directly upstream of the junction. The excess pressure squeezes the neck of the emerging droplet, promoting breakup. The magnitude of the squeezing pressure increases dramatically as the distance between the emerging interface and the opposing wall of the microchannel decreases [1].

Several dimensionless parameters describe microfluidic droplet breakup. These parameters are commonly defined in terms of experimentally controlled variables; connecting the empirical quantities to the governing forces described earlier remains a challenge. The capillary number Ca describes the relative magnitude of the viscous shear stress compared with the capillary pressure. A simple definition for Ca is given in terms of the average velocity u_c of the continuous-phase liquid:

$$\mathrm{Ca} = \frac{\mu_c u_c}{\sigma} = \frac{\mu_c Q_c}{\sigma w_c h}. \tag{1}$$

During a typical experiment, the dispersed- and continuous-phase liquids are injected at different volumetric flow rates, and the ratio of flow rates φ characterizes the contrast between these two speeds:

$$\varphi = \frac{Q_d}{Q_c}. \tag{2}$$

The viscosity ratio λ is an important parameter in droplet breakup, where

$$\lambda = \frac{\mu_d}{\mu_c}. \tag{3}$$

Finally, the numerous geometrical parameters defining a T-junction lead to additional dimensionless ratios characterizing the geometry. For the cases considered in this study there are two aspect ratios, one comparing the width of the continuous-phase inlet channel to the channel depth, w_c/h, and one comparing the inlet widths of the two phases,

$$\Lambda = \frac{w_d}{w_c}. \tag{4}$$

In the present study, in addition to characterizing the role of the capillary number Ca, the flow rate ratio φ, and the viscosity ratio λ on the droplet breakup process in a T-junction, we also characterize the role of the T-junction geometry. We restrict our study to microchannels with fixed depth h, in which the channel widths are larger than the depth, $w_c/h > 1$ and $w_d/h > 1$. We systematically vary the ratio of inlet widths Λ. We note that the influence of inertia and gravity on microfluidic droplet breakup processes is typically negligible [11]. The Reynolds number Re describing the ratio of inertia to viscous stresses and the Weber number We describing the ratio of inertia to capillary forces are both typically small. In the experiments we discuss here, the maximum values of these parameters, based on properties of the continuous-phase liquid, are $\mathrm{Re} = \rho_c u_c D_c/\mu_c \approx 0.08$ and $\mathrm{We} = \rho_c u_c^2 D_c/\sigma \approx 0.01$, where D_c is the hydraulic diameter of the continuous-phase inlet channel. The Bond number $\mathrm{Bo} = \Delta\rho g D_c^2/\sigma$ describing the ratio of body forces to capillary forces is also small, with a value approximately $\mathrm{Bo} \approx 4 \times 10^{-4}$ for our devices, where $\Delta\rho$ is the density difference between the two liquids.

Previous experimental studies of droplet breakup at microfluidic T-junctions have focused on two distinct breakup regimes. In one set of studies, the droplets generated are smaller than the channel width and it is observed that the droplet size depends predominantly on the capillary number Ca and not on the flow rate ratio φ [2,4]. Scaling models developed to describe these experiments assume that the viscous shear stress is the dominant force controlling droplet breakup, and the simple models find reasonable agreement with the experiments [2,4]. A much larger number of studies focus on a different regime in which the droplets fill the channel and form "slug"- or "plug"-like shapes [1,3,21–23]. In this case, it is observed that the droplet length depends predominantly on the flow rate ratio φ and not on the capillary number Ca. Scaling arguments developed to describe these experiments neglect the influence of the viscous shear stress and assume that the dominant force controlling droplet breakup is the squeezing pressure, since the large droplets obstruct the channel. By arguing that detachment begins once the emerging droplet fills the channel and that the droplet keeps growing due to continuous injection of the dispersed-phase liquid, Garstecki and co-workers obtain a relationship between the droplet length L and the flow rate ratio,

$$\frac{L}{w_c} = 1 + \alpha\varphi, \tag{5}$$

where α is a constant of order unity [1,10]. Independent experiments and numerical simulations by van der Graaf and co-workers support the idea of a two-stage growth and detachment process [24]. Other studies produce droplets that appear to lie between these two regimes [24–26]. In all of these studies, the viscous-stress-dominated regime occurs when the capillary number is relatively large ($0.01 < \mathrm{Ca} < 0.5$) and when the continuous-phase channel is wider than

the dispersed-phase channel. The squeezing regime occurs when the capillary number is very low ($Ca<0.01$) and the channel widths are similar.

Most recently, De Menech and co-workers have used a diffuse interface method to numerically simulate droplet breakup in microfluidic T-junctions, focusing on the transition between the squeezing regime and the regime in which viscous shear stress is dominant, which the authors term "dripping" to draw analogy to observations of unconfined droplet dynamics [18]. Examining the influence of the capillary number, flow rate ratio, and viscosity ratio in square channels, a distinct transition between squeezing and dripping is found at a critical capillary number $Ca^* \approx 0.015$, above which the slope of the curve describing the droplet volume as a function of capillary number becomes significantly steeper. In the squeezing regime $Ca<Ca^*$, the droplet size is independent of the viscosity ratio and increases with the flow rate ratio such that the scaling argument of Garstecki and co-workers given by Eq. (5) is observed, with $\alpha=2$. In the dripping regime $Ca>Ca^*$, the droplet size decreases strongly as the capillary number increases. Larger viscosity ratios lead to smaller droplets, and the size is more sensitive to changes in capillary number. The droplet size in this regime is not as strongly dependent on the flow rate ratio. The authors examine pressure fluctuations upstream of the emerging interface in the squeezing and dripping regimes and find that even in the dripping regime the squeezing pressure cannot be neglected since the confinement of the emerging interface always plays a role in the process. Finally, above a capillary number of $Ca^\dagger \approx 0.5$, the detachment point is observed to move gradually downstream as the breakup process transitions to a low-Reynolds-number "jetting" mode similar to that observed in both confined and unconfined droplet breakup [6,27,28]. The transition to jetting occurs at smaller values of $Ca^\dagger$ as the viscosity ratio increases.

The simulations performed by De Menech and co-workers demonstrate that the transition from squeezing to dripping is one of the richest in the operating space of droplet breakup in microfluidic T-junctions, owing to the fact that both the squeezing pressure and the viscous shear stress are important. Despite numerous experimental studies, none have reported detailed studies in this region. In addition, each study utilizes a different T-junction geometry and none systematically explore the influence of the geometry on the droplet breakup dynamics. Nevertheless, we expect the geometry of the T-junction to play a central role in determining the magnitudes of both the squeezing pressure and the viscous shear stress since both forces depend on the distance between the emerging interface and the opposing microchannel wall at any instant in time.

To gain insight into the role of the T-junction geometry on droplet-breakup dynamics, we present a comprehensive experimental study in which we systematically vary the capillary number and flow rate ratio for several channel geometries. We hold fixed the ratio of the continuous-phase channel width to depth, $w_c/h=1/3$, while we vary the width of the dispersed-phase channel from $\Lambda=w_d/w_c=0.4$ to 2.5. For each geometry, we vary the capillary number from Ca $=0.0005$ to 0.3 at a constant flow rate ratio of $\varphi=0.25$. In addition, for one T-junction geometry, we vary the viscosity ratio from $\lambda=1/6$ to $1/350$ (for a fixed flow rate ratio $\varphi=0.25$) and the flow rate ratio from $\varphi=0.05$ to 0.5 (for a fixed viscosity ratio $\lambda=1/100$). Thus, our experiments span the range of conditions considered by De Menech and co-workers, except that our channels are not square. Finally, we develop a scaling model that captures the influence of both squeezing pressure and viscous shear stress by incorporating a force balance on the emerging interface. This simple model indicates that the width ratio Λ is a critical factor in the process. Finally, we discuss the dependence of droplet size and production frequency on viscosity ratio and width ratio.

TABLE I. Physical properties of liquids used in experiments, along with dimensions of the microchannels used.

Fluid system		Viscosity [mPa s]	Device dimensions [μm]	
Continuous phase	Silicone oil	6	w_c	150
		50	w_d	65–375
		100	w_o	150
		350	h	50
Dispersed phase	De-ionized water	1		
Interfacial tension [mN/m]		45.57 ± 0.96		
Volumetric flow rates [μl/h]		4–2000		

II. METHODS AND MATERIALS

The microchannels used in the present study are molded in poly(dimethyl siloxane) elastomer (PDMS, Dow Sylgard 184) using standard soft lithography fabrication [29,30]. To close the microchannels, we first coat a thin layer of PDMS onto a glass microscope slide and then expose the surfaces of both the molded microchannel and the thin PDMS layer to ionizing air plasma (Harrick Scientific). Plasma treatment ensures that the two surfaces bond covalently. The thin layer of PDMS ensures uniform wetting on all microchannel surfaces, and the glass microscope slide provides stability. Prior to use, sealed microchannels are placed in a 180 °C oven for 2 h to ensure that the microchannel surfaces have reverted to hydrophobic wetting.

The microchannel geometries considered in this study are listed in Table I. We select a fixed width $w_c=w_o=150$ μm and vary the width of the dispersed phase inlet channel from $w_d=65$ to 375 μm. Soft lithography leads to microchannels with rectangular cross section and uniform depth throughout. In this study, the depth of all microchannels considered is $h=50$ μm.

In all cases, the dispersed phase liquid is de-ionized water. Low-molecular-weight silicone oil (Gelest) is used as the continuous-phase liquid. Several oils have been selected such that the viscosity μ_c varies while holding the surface tension constant. Viscosity values are used as reported from the manufacturer and are listed in Table I. We use a du Noüy ring tensiometer [31] to measure the interfacial tension of the water-oil pairs, obtaining an average value of $\sigma=45.57 \pm 0.96$ mN/m for all four silicone oil and water com-

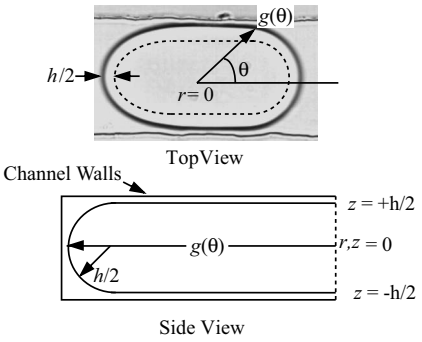

FIG. 2. Top-view projection of a typical droplet imaged via video microscopy. Edge detection is performed to obtain the in-plane droplet shape $g(\theta)$, which is integrated to obtain the projected area of the droplet. In the out-of-plane dimension we assume that the perimeter of the droplet is curved due to surface tension as shown in the side view, with a curvature approximately equal to half the channel depth, $h/2$. Assuming this shape allows integration in three dimensions to obtain an estimate of the droplet volume.

binations considered. We assume that both liquids are free of surface-active contaminants, and no surfactant is added to either liquid.

The two liquids are driven using independent syringe pumps (Harvard Apparatus PHD 2000). Prior to beginning an experiment, the microfluidic device is primed by filling all microchannel segments with the continuous-phase oil. Once primed, the pump for the dispersed-phase liquid is started. The pump for the continuous-phase liquid is started after the dispersed-phase liquid reaches the T-junction. Dimensional values of the volumetric flow rates are selected to achieve the range of capillary numbers and flow rate ratios listed above. For the oil-water pairs selected, the desired dimensionless parameters correspond to volumetric flow rates that range from $Q=4$ to 2000 μl/h. For each new data point corresponding to a pair of flow rates (Q_c, Q_d), the fluids begin at rest so that each experiment is independent of the others.

To ensure steady-state droplet production, data are recorded after at least 30 min has passed from the time that the first droplet is produced. A long equilibration time is needed due to the flexibility of the PDMS, which imparts compliance to the microchannel network and can lead to long initial equilibration times. Using a more rigid material such as glass or silicon would minimize this effect. Once steady-state conditions are achieved, high-speed video of droplet production is captured downstream of the T-junction using a high-speed CMOS camera (IDT XS-4) mounted to an inverted light microscope (Nikon TE 2000-U). Video is analyzed frame by frame in post-processing to quantify droplet breakup parameters including the droplet volume and the frequency of droplet production. In order to obtain reasonable statistics, at least 200 distinct droplets from each experiment are analyzed, since we find that the standard deviation approaches a constant value above this number.

The size of an individual droplet can in principle be measured from a two-dimensional image captured as the droplet passes through the viewing region, such as that shown in Fig. 2. However, obtaining accurate size estimates based on image processing presents several challenges. As shown in the figure, droplets formed at moderate capillary numbers are nearly as wide as the channel, but are not "plug"-like as others have reported at low capillary numbers [1], where the droplet length and width are adequate to accurately describe the droplet size. Nor are the droplets much smaller than the channel so that they can be treated as spheres, or circular cylinders pressed between the top and bottom channel walls. Therefore an accurate analysis of the size of a droplet requires one to account for its more complicated shape. In addition, there is a lack of information about the shape and size of the droplet in the out-of-plane dimension. In the selected channel geometries, the channel depth is smaller than any of the channel widths, suggesting that the droplets should nearly fill the channel in this direction. However, factors such as swelling of the PDMS by the silicone oil [32], flexing of the PDMS in response to a pressure-driven flow [33,34], and the presence of a thin layer of oil surrounding the droplet can lead to significant variability in the droplet size. To circumvent these uncertainties, we obtain a global measurement of the droplet volume by assuming that over the duration of the experiment, the mass of the dispersed-phase liquid injected by the syringe pump must equal the mass contained in the produced droplets. Using high-speed video we can count the total number of droplets, N_d, produced and the total time elapsed, Δt, between the first and last droplets in a given video segment with a high degree of certainty. Thus, the time-averaged droplet volume $\langle V \rangle$ is given by

$$\langle V \rangle = \frac{Q_d \Delta t}{N_d}. \tag{6}$$

While Eq. (6) leads to an accurate and simple measure of the droplet volume, it does not permit quantification of the polydispersity. For this, we analyze individual droplets and make simple assumptions about the droplet shape out of the plane. Individual video frames are post-processed using custom image-analysis software written in MATLAB (The Mathworks, Inc.) to detect the edges and the projected area of each droplet. If both the length and width of the droplet are smaller than the minimum channel dimension, we assume that the droplet is unconfined by the channel walls, and therefore that the droplet is axisymmetric about an axis aligned with the flow direction. In this case, the volume is calculated using the Pappus centroid theorem [35],

$$V = 2\pi \bar{x} A, \tag{7}$$

where V is the volume, $\bar{x}$ is the distance from the axis of symmetry to the centroid of the upper half of the projected area, and A is the area bounded by the upper half of the droplet. The area and centroid of the upper half of the droplet are calculated by applying MATLAB functions for blob analysis to the region of the object identified as the droplet.

If either dimension is larger than the minimum channel dimension, the channel walls confine the droplet, resulting in a more complicated droplet shape. In this case, we assume that the droplet nearly fills the channel and has depth h. In addition, we assume that the edges of the droplet must be curved in order to minimize surface energy. We approximate

this curvature by assuming that, in cross section, the droplet has circular end caps with radius of curvature equal to the half-depth of the droplet $r_c \approx h/2$, as shown in Fig. 2. This assumption leads to the following expression for the three-dimensional shape of the droplet:

$$r(\theta,z) = \left(\frac{h^2}{4} - z^2\right) + g(\theta) - \frac{h}{2}, \tag{8}$$

where r is a function describing the three-dimensional shape of the droplet, z is the out-of-plane coordinate, and $g(\theta)$ is the function describing the edges of the droplet obtained from the captured image. Equation (8) is integrated with respect to z and θ to obtain an expression for the droplet volume:

$$V = \left(\frac{5}{12} - \frac{\pi}{8}\right)\pi h^3 + \left(\frac{\pi}{8} - \frac{1}{2}\right)\pi h^2 \int_0^{2\pi} g(\theta) d\theta + \frac{h}{2}\int_0^{2\pi} g(\theta)^2 d\theta. \tag{9}$$

The integrals in Eq. (9) are calculated by applying a Riemann numerical integration scheme to the droplet boundary data obtained from the captured image [36]. We estimate the droplet depth h in Eq. (9) using the global volume obtained from Eq. (6). Taking the sum of Eq. (9) over the N_d droplets observed in a given experiment leads to a cubic function of the droplet depth in terms of the time-averaged volume $\langle V \rangle$ computed from Eq. (6) and the average values of the integrals over the edge functions $g(\theta)$. Solving the cubic equation yields an effective droplet depth corresponding to the specific experiment. The effective droplet depth is then used in conjunction with Eq. (9) to obtain volume estimates for individual droplets. Finally, we compute the standard deviation σ for this ensemble of values and report the ratio $\sigma/\langle V \rangle$ as a measure of the polydispersity.

In addition to the droplet volume, we independently measure the droplet production frequency f by counting the number of video frames elapsed between droplets entering the observation region and using the formula $f = N_{FR}/N$, where N_{FR} is the frame rate and N is the average number of frames elapsed between droplets.

III. DROPLET BREAKUP IN THE TRANSITION REGION

In order to systematically characterize the transition region between squeezing and dripping, we first select a reference geometry and keep the fluid pair fixed. We measure droplet volume and polydispersity as a function of capillary number and flow rate ratio for the reference system by selecting three different flow rate ratios $\varphi = 0.05$, 0.25, and 0.5. For each fixed flow rate ratio, the capillary number is varied from Ca=0.005 to 0.3, reflecting the range of flow rates that we can practically achieve in experiments. To keep the flow rate ratio fixed, both Q_d and Q_c must vary as Ca varies. Dimensional parameters for the reference system are given in Table I. The width of the dispersed-phase inlet channel is equal to the width of the continuous-phase inlet channel, $w_d = w_c = 150$ μm, such that $\Lambda = 1$. The viscosity of the continuous-phase liquid is $\mu_c = 100$ mPa s, such that $\lambda = 0.01$.

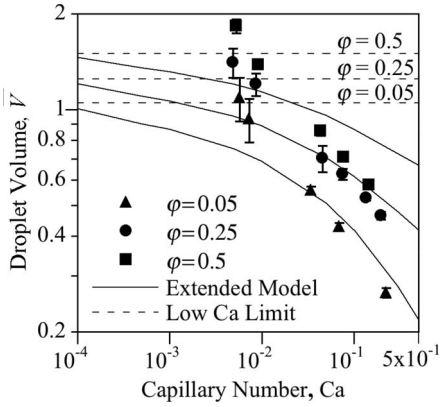

FIG. 3. Dimensionless droplet volume as a function of capillary number for a fixed viscosity ratio $\lambda = 0.01$ ($\mu_c = 100$ mPa s). The microchannel geometry is given by $w_d = w_c = 150$ μm ($\Lambda = 1$), $h = 50$ μm. Solid lines represent droplet volumes predicted by the extended scaling model described in the text, while the dashed lines represent the droplet volume resulting from the low-capillary-number model of Garstecki *et al.* [1]. Each line corresponds to a fixed value of the flow rate ratio, where the lines shift to larger values as the flow rate ratio increases.

In Fig. 3, we plot the dimensionless droplet volume $\bar{V}$, defined as the time-averaged droplet volume $\langle V \rangle$ calculated from Eq. (6) normalized by the quantity $w_c^2 h$. Over the range of flow conditions considered, we observe that the droplet volume decreases as the capillary number increases and the droplet volume increases as the flow rate ratio increases, as shown in Fig. 3. This trend is consistent with many other studies in which droplet production is controlled by two immiscible streams in a variety of different geometries (see, for example, [11] and references therein).

The droplet sizes produced in microfluidic T-junctions are highly uniform. To show this, we organize polydispersity values obtained using the procedure described in Sec. II on an operating diagram in terms of capillary number and flow rate ratio, shown in Fig. 4. For capillary number greater than Ca > 0.025, polydispersity values consistently fall below 2%. For capillary number less than Ca < 0.025 and flow rate ratio less than $\varphi < 0.1$, we observe polydispersity values as high as 10%. As flow rate ratio increases with Ca < 0.025, polydispersity values decrease to between 2% and 6%. The largest fluctuations in the droplet size occur when the volumetric flow rates are lowest, suggesting that the fluctuations may arise from the stepper-motor-driven syringe pumps.

We compare the measured droplet volumes shown in Fig. 3 with existing scaling models corresponding to different modes of droplet breakup. In the squeezing regime, the droplet length should follow Eq. (5) for Ca < 0.01 and thus the droplet volume should be independent of the capillary number below this limit [1]. The constant values of droplet volume corresponding to Eq. (5) for each of the three flow rate ratios considered are shown as dashed lines in Fig. 3, where we have taken $\alpha = 1$. Although most of our experiments lie above Ca=0.01, the measurements below this value show no sign of approaching a constant value as the capillary number

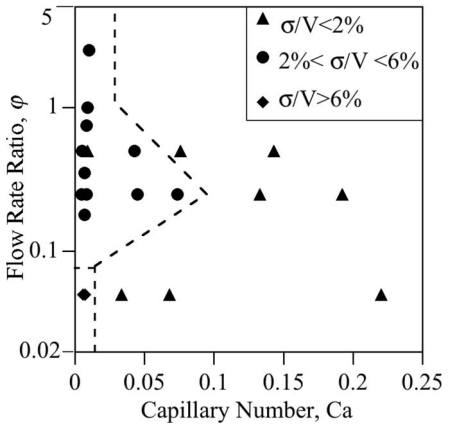

FIG. 4. Operating diagram depicting the polydispersity in the droplet volume as a function of flow rate ratio and capillary number. The polydispersity is computed by taking the ratio of the standard deviation of many measurements of individual droplet volumes to the mean of those measurements.

decreases. We observe that the droplet volume varies with capillary number over the entire range considered. More specifically, we find that the droplet volume exhibits a power-law dependence on the capillary number for these experiments, where $\bar{V} \propto \mathrm{Ca}^{1-\alpha}$ and the power-law exponent is $(1-\alpha) = -0.316 \pm 0.016$ on average.

Although the scaling model of Garstecki and co-workers does not capture the capillary number dependence that we observe, it does capture the observed dependence on the flow rate ratio. To show this, we plot droplet lengths corresponding to the data shown in Fig. 3 as a function of flow rate ratio. We compare these data to the scaling model of Garstecki and co-workers in Fig. 5. For all values of capillary number, the droplet length is clustered around the curve corresponding to Eq. (5), and on average these values gradually increase as flow rate ratio increases. We also perform a

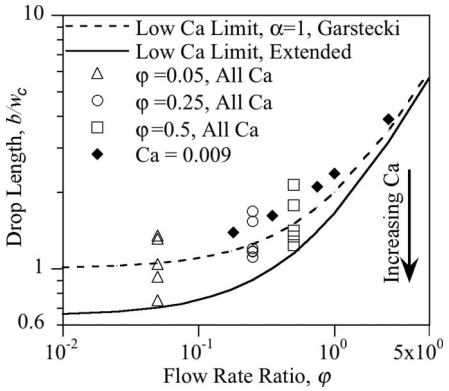

FIG. 5. Comparison of measured droplet lengths corresponding to the experiments shown in Fig. 3 ($\lambda = 0.01$, $w_d = w_c = 150$ μm, $h = 50$ μm) with the low-capillary-number model of Garstecki *et al.* [1] shown as a dashed line and the extended model described in the text shown as a solid line corresponding to Ca=0.009. Although we observe that droplet sizes always decrease with increasing capillary number, the dependence on the flow rate ratio is similar to that predicted for the purely squeezing regime.

set of experiments corresponding to a small fixed capillary number Ca=0.009 for a wider range of flow rate ratios up to $\varphi = 2.5$. These measurements, represented by solid symbols in Fig. 5, agree reasonably well with the scaling model at low capillary number, although the model slightly underpredicts the droplet length. We note that Garstecki and coworkers state that the scaling model should hold as long as the width of the dispersed-phase inlet channel is greater than half the width of the continuous-phase inlet channel, $\Lambda > 0.5$, and all of the present experiments meet this criterion.

Since the majority of our experiments lie above the critical capillary number Ca=0.01, we expect that the viscous shear stress will play an increasingly important role in the breakup process. The simplest scaling argument in this regime assumes that droplets break when the viscous shear stress overcomes the interfacial tension, analogous to droplet breakup in unconfined systems [37–39]. Thorsen and coworkers compare their measured droplet sizes with this scaling argument, estimating the shear stress by measuring the gap between the emerging interface and the opposing wall at the point of breakup. This scaling argument systematically overpredicts the measured sizes [2]. More recently, Husny and Cooper-White developed an alternate scaling model based on the same basic idea [4]. In this case, the authors assume that the confinement of the emerging droplet is negligible and that droplets pinch off when the cross-flow drag on the emerging interface exceeds the capillary force. The model results in a fourth-order polynomial for the predicted droplet diameter as a function of 1/Ca, and it agrees well with measurements in T-junctions with $w_c \gg w_d$ for capillary numbers up to Ca=0.4. We do not make a direct comparison with the droplet breakup model of Husny and Cooper-White, since the resulting equation leads to complex values for the droplet diameter at our experimental conditions. The experiments of Husny and Cooper-White considered larger viscosity ratios and smaller ratios of the inlet channel widths. In any case, this model predicts that droplet size is independent of flow rate ratio, which is inconsistent with our observations in the same capillary number range.

Our experiments correspond most closely with the recent numerical simulations of De Menech and co-workers [18], in which the ratio of the inlet channel widths is order unity and the range of capillary numbers and flow rate ratios considered is similar to ours. Like De Menech *et al.*, we observe that the droplet volumes depend on *both* the capillary number and the flow rate ratio. However, at the viscosity ratio selected for our reference system, which is significantly smaller than values considered in the simulations, we do not observe the change in slope at a critical capillary number of Ca=0.015 that was found in the simulations. As shown in Fig. 3, we observe that the droplet volume continues to increase as the capillary number decreases significantly below this critical value. Clearly, droplet breakup in microfluidic T-junctions is complicated in the intermediate regime where both squeezing pressure and viscous shear stress play an important role. In addition, it appears that factors such as the viscosity ratio and the microchannel geometry have not been adequately accounted for in the experimental, theoretical, and numerical studies reported to date.

IV. EXTENDED SCALING MODEL FOR DROPLET BREAKUP IN THE TRANSITION REGION

The existing scaling models described earlier agree well with experiments at conditions corresponding to a given mode of droplet breakup. Motivated by the success of these models, we seek a simple model describing the transition region that combines the salient features of each approach. Garstecki *et al.* assume that detachment of the neck begins when the emerging droplet fills the continuous-phase channel and that the resulting droplet size is governed by the rate of thinning of the neck and the rate of filling of the droplet during detachment [1]. This assumption is consistent with observations for "plug"-like droplets. However, in our experiments, where squeezing is clearly not the only mechanism for breakup, droplets are smaller than the continuous-phase channel, so detachment must begin before the emerging droplet has completely filled the channel. We assume, similar to Thorsen *et al.*[2] and Husny and Cooper-White [4], that the size of the emerging droplet prior to the onset of detachment is determined not by the width of the junction region, but rather by the balance of the three primary forces that govern the droplet breakup process: the capillary force resisting deformation of the interface, the viscous stress acting on the emerging droplet, and the squeezing pressure. Once the sum of the viscous stress and the squeezing pressure exceed the capillary pressure, detachment begins. During detachment, the rate of thinning of the neck and the rate of filling of the droplet control additional growth of the droplet.

To quantify these arguments, we define several relevant dimensions. The length of the emerging droplet as measured from the downstream corner of the T-junction is denoted b as shown in Fig. 1. We assume that the extent of the droplet across the width of the channel is approximately equal to b at early times. As long as the channel depth h is smaller than the dispersed-phase channel width w_d, we assume that the droplet completely fills the channel depth. We denote the width of the neck s as shown in Fig. 1, and we assume that the initial width of the neck is equal to the width of the dispersed-phase inlet channel. Using these parameters we can estimate the magnitudes of the relevant forces, guided by estimates originally provided by Garstecki *et al.* [1].

The capillary force is given by the difference between the Laplace pressures at the upstream and downstream ends of the emerging droplet multiplied by the projected area of the emerging interface bh. The mean curvature at the downstream end of the droplet is given by the sum of the curvature in the cross-channel direction $2/b$ and the curvature in the depth direction $2/h$. The mean curvature at the upstream end of the droplet is given by the sum of the in-plane curvature near the neck, which we approximate as $1/b$, somewhat smaller than the curvature at the downstream end, and the curvature in the depth direction. The resulting capillary force F_σ is given by

$$F_\sigma \approx \left[-\sigma\left(\frac{2}{b}+\frac{2}{h}\right)+\sigma\left(\frac{1}{b}+\frac{2}{h}\right)\right]bh \approx -\sigma h. \quad (10)$$

We note that the capillary force is negative, stabilizing the droplet against breakup.

The product of the viscous stress acting on the emerging interface and the projected area of the emerging interface approximates the viscous shear force F_τ. The viscous stress is given by the product of the continuous-phase viscosity and the effective shear rate in the continuous-phase liquid as it passes between the emerging droplet and the opposing channel wall. We approximate the shear rate by taking the ratio of the velocity of the continuous-phase liquid in the gap divided by the gap width, where the gap width is given by the quantity (w_c-b). The resulting viscous force F_τ is given by

$$F_\tau \approx \mu_c \frac{u_{gap}}{(w_c-b)}bh \approx \mu_c \frac{Q_c}{h(w_c-b)^2}bh \approx \frac{\mu_c Q_c b}{(w_c-b)^2}. \quad (11)$$

We estimate the squeezing pressure arising from the obstruction of the channel by the emerging droplet in a similar way to Garstecki *et al.* [1], using the characteristic pressure arising from a lubrication analysis for pressure-driven flow in a thin gap with aspect ratio $(w_c-b)/b$. As the authors note, a detailed lubrication analysis may lead to somewhat different scaling if the shape of the interface is considered [40]. The resulting force F_p due to the squeezing pressure is given by

$$F_p \approx \Delta p_c bh \approx \frac{\mu_c u_{gap}}{(w_c-b)}\frac{b}{(w_c-b)}bh \approx \frac{\mu_c Q_c b^2}{(w_c-b)^3}. \quad (12)$$

We note that Eqs. (11) and (12) are singular as b approaches w_c, or as the droplet approaches the opposing wall of the junction. In our experiments this limit is not reached since the droplets do not completely fill the channel. The idea behind this simple model is that the forces given by Eqs. (11) and (12) become large enough to exceed the stabilizing capillary force as the droplet width b grows and the gap thins. Therefore, we estimate the size of the emerging droplet prior to the onset of detachment by solving for b when the three forces described by Eqs. (10)–(12) sum to zero. In dimensionless terms, the droplet size at the onset of detachment is given by

$$(1-\bar{b})^3 = \bar{b} \times \mathrm{Ca}, \quad (13)$$

where $\bar{b} \equiv b/w_c$. Thus we see that the capillary number emerges as the controlling parameter for the initial size of the droplet prior to the onset of detachment.

To obtain the final droplet length at detachment, we incorporate an argument similar to that of Garstecki *et al.* [1] during the detachment process. We assume that the average velocity of the continuous-phase liquid exerting the squeezing pressure on the interface governs the thinning rate of the neck, such that $u_{squeeze} \approx u_c = Q_c/w_c h$. During the squeezing process, the dispersed-phase liquid is continually injected such that the velocity of the emerging tip of the droplet can be approximated by $u_{growth} \approx Q_d/bh = u_d \Lambda/\bar{b}$, where $u_d = Q_d/w_d h$. The added length of the droplet from the onset of thinning to detachment is estimated by the product of the time required for the neck to thin to zero, $t_{squeeze}$

$\approx w_d/u_{squeeze}$, and the velocity of the tip of the droplet. Combining these expressions we obtain an expression for the final dimensionless length $\bar{L}=L/w_c$ of the droplet:

$$\bar{L} \approx \bar{b} + \frac{\Lambda}{\bar{b}}\varphi. \tag{14}$$

Equation (14) is equivalent to Eq. (5) except that in the model of Garstecki *et al.*, $\bar{b}=1$ and the fitting constant α replaces the width ratio Λ.

To compare with our experiments, we estimate the droplet volume by $V \approx Lbh$ such that the dimensionless volume is given by

$$\bar{V} = \frac{V}{w_C^2 h} \approx \bar{L}\bar{b} \approx \bar{b}^2 + \Lambda\varphi. \tag{15}$$

Thus, to estimate the droplet volume for a given set of experiment conditions, one must first calculate b using Eq. (13) and then calculate the droplet volume using Eq. (15). Several appealing features are evident in this model. First, the predicted droplet volume depends on both the capillary number and the flow rate ratio, consistent with our observations. For small capillary number, the model of Garstecki *et al.* is recovered if $\alpha=\Lambda$, since $\bar{b}\to 1$. Additionally, the width ratio Λ emerges as a parameter characterizing the role of geometry in the breakup process.

The predicted volume calculated using Eqs. (13) and (15) for $\Lambda=1$ is shown in Fig. 3 for the same conditions considered in the experiments. At low capillary number, the predicted volume approaches a constant value identical to that predicted by Garstecki *et al.* As the capillary number increases, the droplet volume decreases and the slope gradually becomes steeper, consistent with the change in slope described by De Menech *et al.* [18]. While our approximate model does not exhibit an obvious "critical capillary number" marking a transition between the two droplet-breakup regimes, the slope begins to increase in the neighborhood of Ca=0.01, consistent with critical values reported by others [1,18]. In Fig. 5, we plot the predicted droplet length as a function of flow rate ratio for Ca=0.009, the same value considered in experiments. Similar to the model of Garstecki *et al.*, the predicted length approaches a constant value at low flow rate ratio and then increases as flow rate ratio increases. For the finite capillary number considered, the predicted length is smaller than that given by Eq. (5), and the two model curves converge at high flow rate ratios.

These results are consistent with the physical idea that the squeezing pressure should be the predominant factor in droplet breakup at both low capillary numbers and high flow rate ratios, while at larger capillary number and lower flow rate ratios the viscous stress should play a more important role. However, while the approximate model appeals to many of our physical expectations for the droplet-breakup process, the predicted droplet sizes agree only qualitatively with our experiments for the reference system. For example, the measured droplet volumes shown in Fig. 3 do not approach a constant value at low capillary number and the measured values decrease more rapidly than predicted as capillary number increases. In Fig. 5, the approximate model underpredicts the measured droplet length. There are many possible sources of discrepancy between the assumptions inherent in the described model and the dynamics of droplet breakup in a real experiment. To validate these assumptions and develop a more robust model is outside the scope of the present paper. On the other hand, the simple model we have described captures many salient features of our observations and suggests that additional factors should play a role, consistent with our intuition. In the next section, we examine experimentally the role of the viscosity ratio, which does not appear in the approximate model, but is important in droplet-breakup processes, and the width ratio of the T-junction, which appears in the approximate model.

V. INFLUENCE OF FLUID PROPERTIES AND GEOMETRY ON DROPLET BREAKUP

Existing studies of droplet breakup in T-junctions have focused mainly on the role of the volumetric flow rates on the breakup process. Two additional parameters have not been examined in detail experimentally: the viscosity ratio and the ratio of channel widths, $\Lambda=w_d/w_c$. Although existing models do not include viscosity ratio as a parameter, numerical simulations indicate that the droplet size depends on viscosity ratio when the viscosities are similar [18]. The effect is most pronounced in the dripping regime and diminishes as squeezing takes over. In experiments, Tice *et al.* [22] and Guillot and Colin [27] report that the viscosity ratio plays a role in the transition to jetting, but its influence has not been systematically examined near the squeezing-to-dripping transition. Of course, the viscosity ratio is known to influence breakup of isolated droplets [41] and liquid jets [42].

While the viscosity ratio does not appear in current models, the width ratio of the T-junction, $\Lambda=w_d/w_c$, appears as a new parameter in the approximate scaling model described in Sec. IV. This is appealing since we and others have argued that confinement of the emerging droplet by the opposing channel wall is important to droplet breakup [1,18]. In particular, we expect the squeezing pressure to become increasingly important as the distance over which the droplet grows before encountering a wall, w_c, becomes relatively small compared with the initial diameter of the droplet, w_d. Thus, confinement of the emerging droplet is more pronounced as the width ratio increases. At the other extreme, studies that have considered very small width ratios ($w_c \gg w_d$) report that the resulting droplet size is independent of flow rate ratio [4], indicating that squeezing pressure is significantly less important when the droplet is relatively unconfined. Equation (15) supports this hypothesis since the second term containing the flow rate ratio vanishes as the width ratio goes to zero.

In this section, we examine the role of both viscosity ratio and width ratio in the droplet breakup process. To vary the viscosity ratio we choose among several silicone oils for the continuous-phase liquid (cf. Table I). De-ionized water is the dispersed-phase liquid in all cases, resulting in viscosity ratios below unity. For each fluid pair, we measure droplet volume as a function of capillary number for fixed flow rate ratio, $\varphi=0.25$. For small viscosity ratio, we are limited to

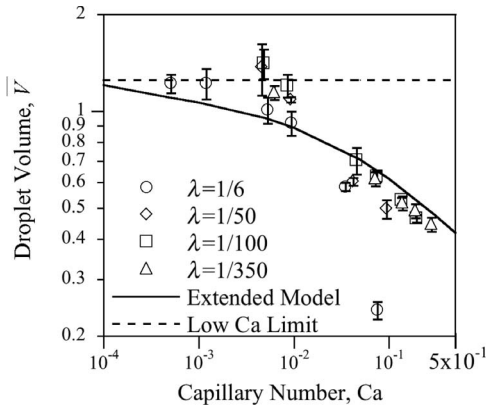

FIG. 6. Dimensionless droplet volume as a function of capillary number for a fixed flow rate ratio $\varphi=0.25$ and four different viscosity ratios. For comparison, the low-capillary-number model of Garstecki *et al.* [1] is shown as a dashed line and the extended model described in the text is shown as a solid line.

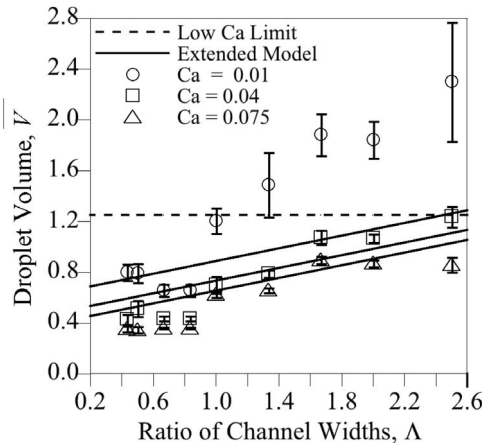

FIG. 7. Dimensionless droplet volume as a function of the ratio of inlet channel widths at fixed flow rate ratio $\varphi=0.25$ and fixed viscosity ratio $\lambda=0.01$ for three different capillary numbers. The width ratio was adjusted by changing the magnitude of the dispersed-phase channel width from $w_d=65$ μm to 375 μm while holding the continuous-phase channel width fixed at $w_c=150$ μm. The dashed line corresponds to the droplet volume predicted by Garstecki *et al.* [1], and the solid lines correspond to the extended scaling model described in the text. The model curves shift down as the capillary number increases, such that the top line corresponds to Ca=0.01, the middle line corresponds to Ca=0.04, and the bottom line corresponds to Ca=0.075.

Ca$>$0.01 due to syringe pump limitations. For large viscosity ratio, we are limited to Ca$<$0.1 to avoid leakage near tubing interconnections. To test the hypothesis that confinement influences droplet breakup, we vary the width ratio by fixing the width of the continuous-phase channel and varying the width of the dispersed-phase channel from w_d =65 to 375 μm, resulting in width ratios from $\Lambda=0.43$ to 2.5. For each width ratio, we report experiments at three capillary number values Ca=0.01, 0.04, and 0.075, for fixed flow rate ratio $\varphi=0.25$, and fixed viscosity ratio $\lambda=0.01$. We note that we consider only geometries in which the channel widths are similar and the droplet is relatively confined.

Figure 6 shows the measured droplet volume as a function of capillary number for four different viscosity ratios (note that the case $\lambda=0.01$ is the same as the reference case; cf. Fig. 3). For all cases except the largest viscosity ratio, the measured droplet volume is nearly independent of the viscosity ratio. The droplet volume decreases as the capillary number increases, exhibiting power-law behavior with an average fitted power-law exponent of $(1-\alpha)=-0.289\pm0.011$. The droplet volume does not approach a constant value at low capillary number over the range of values tested. However, the system with the largest viscosity ratio (the most similar viscosities), $\lambda=1/6$, exhibits markedly different behavior as shown in Fig. 6. At low capillary number, the droplet volume approaches a constant value and decreases with increasing capillary number above Ca$>$0.005. The rate of decrease of the droplet volume at large capillary number is steeper for the larger viscosity ratio. Finally, we observe a transition to jetting for $\lambda=1/6$, in which the detachment point moves downstream as capillary number increases.

Figure 7 shows the measured droplet volume as a function of width ratio for three Ca values. Consistent with earlier observations the volume decreases with increasing Ca. At small width ratio ($\Lambda<1$) the measured volume is approximately constant. As the width ratio increases above $\Lambda>1$, the volume increases approximately linearly with width ratio. The droplet volume is most sensitive to width ratio for low Ca values, increasing by a factor of 2 for Ca=0.075 and a factor of 3 for Ca=0.01.

Comparing the measured droplet volume in Fig. 6 with the scaling model described in Sec. IV, we find that the predicted droplet volume (solid line in the figure) agrees reasonably well with experiments for $\lambda=1/6$ and $\varphi=0.25$ over the range of capillary numbers tested. For the lower viscosity ratios, the model underpredicts the slope at higher capillary numbers. This change in slope is consistent with the numerical simulations of De Menech *et al.*[18]. The dashed line in Fig. 6 represents the low-capillary-number limit predicted from Eqs. (5) and (14), which agrees with observations for $\lambda=1/6$, while no plateau is reached for lower viscosity ratios. Last, Eq. (15) predicts that the droplet volume increases linearly with channel width ratio, with a slope that is independent of Ca. The prediction agrees reasonably well with experiments for the two larger Ca values, while the droplet volume increases more rapidly than predicted for Ca=0.01, as shown in Fig. 7. For comparison, the dashed line represents the prediction from Eq. (5) for $\alpha=1$, which does not explicitly depend on the width ratio and generally overpredicts the volume.

VI. RATE OF DROPLET PRODUCTION

In addition to the droplet volume, the rate of droplet production is an important quantity in the design of microfluidic devices. Mass conservation dictates that the product of the droplet production frequency f and the average droplet volume $\langle V\rangle$ equals the injected volumetric flow rate of the dispersed-phase liquid [19]:

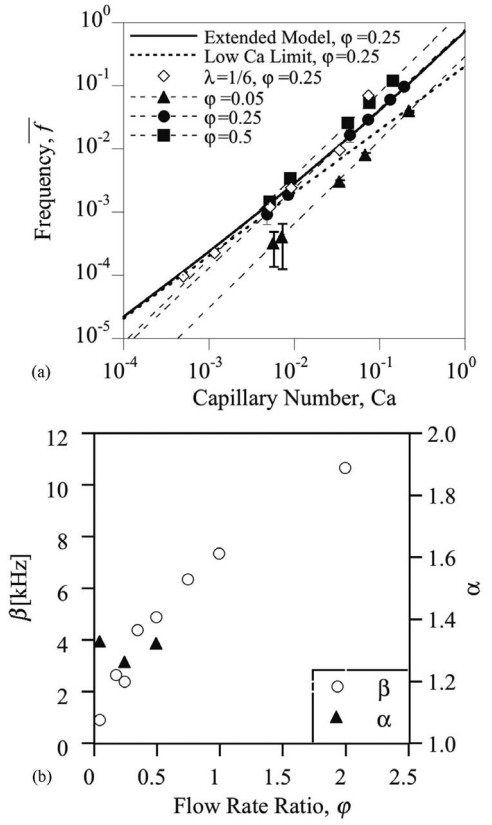

FIG. 8. (a) Droplet production frequency as a function of capillary number for three fixed flow rate ratios corresponding to $\lambda=0.01$ and also for $\varphi=0.25$ and $\lambda=1/6$. Thin dashed lines represent power-law fits to the data, the thicker dashed line represents the low-capillary-number model of Garstecki *et al.* [1], and the solid line represents the extended model described in the text. (b) Fitted values of the power-law exponent α and the constant coefficient β for the experiments shown in part (a). Additional β values have been obtained for the Ca=0.009 data shown in Fig. 5 assuming α is constant.

$$Q_d = f\langle V\rangle. \tag{16}$$

Scaling the droplet production frequency with the capillary-breakup time $t_{cap} \equiv \mu_c w_c/\sigma$, such that $\bar{f} \equiv f t_{cap}$, Eq. (16) becomes

$$\bar{f} = \frac{\mathrm{Ca}\times\varphi}{\bar{V}}, \tag{17}$$

indicating an inverse relationship between the observed frequency and the droplet volume. To validate this relationship, we measure the droplet production frequency as described in Sec. II for experiments corresponding to Figs. 3, 6, and 7. The results are shown in Fig. 8(a) for two viscosity ratios $\lambda=1/100$ and $\lambda=1/6$, where the capillary-breakup time in each case is $t_{cap}=0.33$ ms and 19.8 μs, respectively, and the characteristic frequencies are $f_{cap}=1/t_{cap}\approx 3000$ Hz and 51 000 Hz. As the figure shows, the measured frequency increases with capillary number. For $\lambda=1/6$, the frequency increases more slowly at low Ca, then more rapidly at higher Ca. For low viscosity ratios, the frequency exhibits power-law behavior over the range of Ca considered.

Figure 6 indicates that the measured droplet volume for $\lambda=1/6$ agrees reasonably well with values predicted from Eq. (15). Figure 8(a) shows that the measured frequency for this case also agrees well with the predicted frequency obtained by combining Eqs. (17) and (15). Furthermore, at low capillary number the frequency approaches a linear dependence on Ca, which is consistent with previous studies in the squeezing regime [43] and with the scaling model appropriate for this limit, obtained by combining Eqs. (5) and (17), as shown by the dashed line in the figure. At higher capillary numbers, corresponding to the dripping regime, the frequency increases faster than linear since the droplet volume decreases with increasing Ca.

At low viscosity ratios, the frequency exhibits power-law behavior. In Fig. 8(a), dotted lines represent power-law fits of the form

$$\bar{f} = \bar{\beta}\times \mathrm{Ca}^{\alpha}, \tag{18}$$

where $\bar{\beta}=\beta t_{cap}$ and the power-law exponent is $\alpha=1.31\pm0.03$ on average for all viscosity ratios except $\lambda=1/6$. As the viscosity ratio increases, the exponent increases slightly from $\alpha=1.21$ at $\lambda=1/350$ to $\alpha=1.32$ at $\lambda=1/50$.

Combining Eqs. (17) and (18) results in an expected power-law dependence of droplet volume on Ca given by

$$\bar{V} = \frac{\varphi}{\bar{\beta}}\mathrm{Ca}^{1-\alpha}. \tag{19}$$

In other words, based on fits to the measured frequency data, we expect to find that the droplet volume decreases with capillary number with a power-law exponent equal to $1-\alpha=-0.31\pm0.03$ at low viscosity ratios. This exponent agrees well with the value of $1-\alpha=-0.289\pm0.011$ that was found in Sec. V from power-law fits to the droplet volume data. We have thus shown that for all viscosity ratios considered, the droplet volume and production frequency are linked via mass conservation, as expected.

Finally, we examine the dependence of the coefficient β on system parameters for the low-viscosity-ratio systems. The fitted values of α and β are shown in Fig. 8(b) as a function of flow rate ratio. As the figure shows, the value of α is approximately constant, while β increases with flow rate ratio. β values for higher flow rate ratios are obtained using the data corresponding to Ca=0.009 (cf. Fig. 5), assuming that α is held fixed at the average measured value. The value of β also increases with increasing viscosity ratio. In dimensionless terms, the coefficient increases from $\bar{\beta}=0.70$ for $\lambda=1/350$ to $\bar{\beta}=1.13$ for $\lambda=1/50$, suggesting that β represents a characteristic frequency for the system that is comparable to the capillary breakup frequency. Last, Fig. 9 shows that β decreases nonlinearly with increasing width ratio Λ, approaching a constant value of approximately $\beta\approx 2340$ Hz for $\Lambda>1$. Over the same range, the power-law exponent α remains approximately constant with an average value of $\alpha=1.33\pm0.05$.

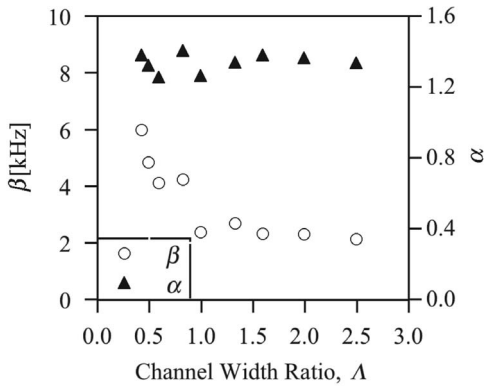

FIG. 9. Fitted values of the power-law exponent α and the constant coefficient β corresponding to the droplet production frequency as a function of the ratio of channel widths. Experiments were performed at fixed flow rate ratio $\varphi=0.25$ and fixed viscosity ratio $\lambda=0.01$. The width ratio was adjusted by changing the magnitude of the dispersed-phase channel width w_d while holding the continuous-phase channel width fixed.

VII. CONCLUSIONS

In this paper, we report a systematic experimental study of droplet breakup at T-shaped microfluidic junctions for conditions near the transition from squeezing dominated pinchoff to dripping, where the viscous shear stress becomes increasingly important. We produce highly uniform droplets with polydispersity less than 2% over a wide range of capillary numbers and flow rate ratios that encompass the transition region reported by others in experiments [1] and numerical simulations [18]. We find that the measured droplet sizes always depend on both capillary number and flow rate ratio, in contrast to previous experimental studies that focus on either a purely squeezing regime, in which droplet size is independent of capillary number, or a purely dripping regime, in which droplet size is independent of flow rate ratio.

We consider several fluid systems in which there is a large contrast between the two liquid viscosities and one system in which the viscosities are similar. For the systems with high viscosity contrast, we do not observe a transition to squeezing over the range of capillary numbers that we were able to explore. In fact, the droplet volume exhibits power-law behavior over this range, decreasing approximately as $V \propto \mathrm{Ca}^{-1/3}$. Independent measurements of the droplet production frequency also indicate power-law behavior for these systems, where the frequency increases at a rate faster than linear with capillary number, $f \propto \mathrm{Ca}^{4/3}$. These two independent observations are consistent with the requirement that the mass of the dispersed phase liquid be conserved. The power-law behavior is independent of viscosity ratio from $\lambda = 1/50$ to $1/350$. Of course, the lack of an observed transition to squeezing in these systems does not rule out the possibility that such a transition exists at lower capillary numbers than we were able to achieve. Pump limitations prevented measurement of capillary numbers significantly below the previously reported critical capillary number of $\mathrm{Ca} \approx 0.01$.

For the system with similar viscosities, $\lambda = 1/6$, the behavior is markedly different. In this system, the droplet volume approaches a constant value as the capillary number decreases, although the transition is more gradual than that reported in recent numerical simulations for similar viscosity ratios [18]. In addition, the critical capillary number is approximately a factor of 10 smaller than the previously reported value of $\mathrm{Ca} \approx 0.01$. At higher capillary numbers, the droplet volume decreases sharply as the capillary number increases, and we observe a transition to jetting in the experiments, where the detachment point moves downstream of the corner.

We describe a physical model that captures several trends observed in experiments. We assume that the sum of forces on the emerging interface due to squeezing pressure and viscous shear stress determines the extent of droplet growth before the neck begins to thin and detach. Once detachment begins, we use arguments similar to those of Garstecki *et al.* [1] to account for continued injection into the droplet during thinning. The resulting scaling model indicates that the droplet volume depends on both capillary number and flow rate ratio, and predicts a low-capillary-number limit identical to that demonstrated theoretically and numerically by Garstecki *et al.* For higher capillary numbers the model consistently underpredicts the slope of the curve for all cases. Since the high-viscosity-contrast systems do not exhibit a low-Ca plateau, the model quantitatively disagrees with these experiments over the entire range considered in experiments. However, the model agrees reasonably well with experiments at low capillary number when the viscosities are similar. Neither our model nor any other existing scaling model contains the viscosity ratio as a parameter, yet the influence of the inner liquid appears to be important to the droplet-breakup process.

Despite its deficiencies, the scaling model also contains the width ratio of the T-junction, a parameter that is not present in earlier models. Intuitively, the channel geometry should play a role in the droplet-breakup process since the squeezing pressure becomes significant when the emerging droplet obstructs the channel. Of course, the viscous stress also increases as the gap between the emerging interface and the opposing wall decreases. The simple model predicts that the droplet volume increases linearly with width ratio, and indeed this behavior is observed in experiments when the capillary number is not too small. For smaller capillary numbers approaching the squeezing-to-dripping transition, the droplet volume increases more dramatically with the width ratio than predicted. Thus, both experiments and scaling arguments support the hypothesis that the T-junction geometry strongly influences the droplet-breakup process.

In summary, we present experiments and scaling arguments demonstrating that the droplet-breakup process in microfluidic T-junctions, while complicated, can be described in terms of the two dimensionless parameters describing the flow: the capillary number and the flow rate ratio; the fluid properties, described by the viscosity ratio; and the geometry of the device, described by several different aspect ratios including the ratio of widths of the inlet channels. The results presented here should enable the design of microfluidic devices that can operate over a wider range of conditions, as well as the development of more detailed models of the droplet-breakup process, especially near the transition from

squeezing-dominated breakup to viscous-stress-dominated breakup.

ACKNOWLEDGMENTS

This research was partially supported by the Donors of the American Chemical Society Petroleum Research Fund and the Pennsylvania Infrastructure Technology Alliance. G.F.C. acknowledges support from ICES and Phillip L. and Marsha Dowd. In addition, we thank the Colloids, Polymers and Surfaces Laboratory and the CMU MEMS Laboratory for use of these facilities for device fabrication and fluid characterization. We are grateful to Lynn Walker, Steve Garoff, Howard Stone, James Schneider, and Alan McGaughey for insightful comments that have led to significant improvements to this work.

[1] P. Garstecki, M. J. Fuerstman, H. A. Stone, and G. M. Whitesides, Lab Chip **6**, 437 (2006).
[2] T. Thorsen, R. W. Roberts, F. H. Arnold, and S. R. Quake, Phys. Rev. Lett. **86**, 4163 (2001).
[3] J. D. Tice, H. Song, A. D. Lyon, and R. F. Ismagilov, Langmuir **19**, 9127 (2003).
[4] J. Husny and J. J. Cooper-White, J. Non-Newtonian Fluid Mech. **137**, 121 (2006).
[5] C. Cramer, P. Fischer, and E. J. Windhab, Chem. Eng. Sci. **59**, 3045 (2004).
[6] A. S. Utada, E. Lorenceau, D. R. Link, P. D. Kaplan, H. A. Stone, and D. A. Weitz, Science **308**, 537 (2005).
[7] S. L. Anna, N. Bontoux, and H. A. Stone, Appl. Phys. Lett. **82**, 364 (2003).
[8] S. L. Anna and H. C. Mayer, Phys. Fluids, **18**, 121512 (2006).
[9] P. Garstecki, I. Gitlin, W. DiLuzio, G. M. Whitesides, E. Kumacheva, and H. A. Stone, Appl. Phys. Lett. **85**, 2649 (2004).
[10] P. Garstecki, H. A. Stone, and G. M. Whitesides, Phys. Rev. Lett. **94**, 164501 (2005).
[11] G. F. Christopher and S. L. AnnaJ. Phys. D **40**, R319 (2007).
[12] S. Sugiura, M. Nakajima, H. Itou, and M. Seki, Macromol. Rapid Commun. **22**, 773 (2001).
[13] D. Dendukuri, K. Tsoi, T. A. Hatton, and P. S. Doyle, Langmuir **21**, 2113 (2005).
[14] T. Nisisako, T. Torii, T. Takahashi, and Y. Takizawa, Adv. Mater. (Weinheim, Ger.) **18**, 1152 (2006).
[15] S. Q. Xu, Z. H. Nie, M. Seo, P. Lewis, E. Kumacheva, H. A. Stone, P. Garstecki, D. B. Weibel, I. Gitlin, and G. M. Whitesides, Angew. Chem., Int. Ed. **44**, 724 (2005).
[16] H. Song, D. L. Chen, and R. F. Ismagilov, Angew. Chem., Int. Ed. **45**, 7336 (2006).
[17] H. Song, J. D. Tice, and R. F. Ismagilov, Angew. Chem., Int. Ed. **42**, 768 (2003).
[18] M. De Menech, P. Garstecki, F. Jousse, and H. A. Stone, J. Fluid Mech. **595**, 141 (2008).
[19] T. Ward, M. Faivre, M. Abkarian, and H. A. Stone, Electrophoresis **26**, 3716 (2005).
[20] R. Dreyfus, P. Tabeling, and H. Willaime, Phys. Rev. Lett. **90**, 144505 (2003).
[21] T. Cubaud, M. Tatineni, X. L. Zhong, and C. M. Ho, Phys. Rev. E **72**, 037302 (2005).
[22] J. D. Tice, A. D. Lyon, and R. F. Ismagilov, Anal. Chim. Acta **507**, 73 (2004).
[23] B. Zheng, J. D. Tice, and R. F. Ismagilov, Anal. Chem. **76**, 4977 (2004).
[24] S. van der Graaf, T. Nisisako, C. Schroen, R. G. M. van der Sman, and R. M. Boom, Langmuir **22**, 4144 (2006).
[25] T. Nisisako, S. Okushima, and T. Torii, Soft Mater. **1**, 23 (2005).
[26] J. H. Xu, S. W. Li, J. Tan, Y. J. Wang, and G. S. Luo, AIChE J. **52**, 3005 (2006).
[27] P. Guillot and A. Colin, Phys. Rev. E **72**, 066301 (2005).
[28] D. F. Zhang and H. A. Stone, Phys. Fluids **9**, 2234 (1997).
[29] D. C. Duffy, J. C. McDonald, O. J. A. Schueller, and G. M. Whitesides, Anal. Chem. **70**, 4974 (1998).
[30] G. M. Whitesides and A. D. Stroock, Phys. Today **54**(6), 42 (2001).
[31] W. D. Harkins and H. F. Jordan, J. Am. Chem. Soc. **52**, 1751 (1930).
[32] S. Venkatraman, A. Nixon, and A. Highe, J. Appl. Polym. Sci. **52**, 1619 (1994).
[33] D. Dendukuri, S. S. Gu, D. C. Pregibon, T. A. Hatton, and P. S. Doyle, Lab Chip **7**, 818 (2007).
[34] M. A. Holden, S. Kumar, A. Beskok, and P. S. Cremer, J. Micromech. Microeng. **13**, 412 (2003).
[35] W. F. Kern and J. R. Bland, *Theorem of Pappus*, in Solid Mensuration with Proofs, 1948 (Wiley, New York, 1948), pp. 110–115.
[36] H. Kestelman, in *Modern Theories of Integration* (Dover, New York, 1960), pp. 33–66.
[37] J. M. Rallison, Annu. Rev. Fluid Mech. **16**, 45 (1984).
[38] H. A. Stone, Annu. Rev. Fluid Mech. **26**, 65 (1994).
[39] G. I. Taylor, Proc. R. Soc. London, Ser. A **146**, 501 (1934).
[40] H. A. Stone, Chem. Eng. Sci. **60**, 4838 (2005).
[41] B. J. Bentley and L. G. Leal, J. Fluid Mech. **167**, 241 (1986).
[42] S. Tomotika, Proc. R. Soc. London, Ser. A **150**, 322 (1935).
[43] T. Nisisako, T. Torii, and T. Higuchi, Lab Chip **2**, 24 (2002).